CMS Physics Analysis Summary

Contact: cms-pag-conveners-susy@cern.ch 2016/08/04

Search for supersymmetry in final states with at least one photon and $E_{\mathrm{T}}^{\mathrm{miss}}$ in pp collisions at $\sqrt{s} = 13$ TeV

The CMS Collaboration

Abstract

A search for electroweak production of gauginos is presented using the first LHC Run II data at a center-of-mass energy of 13 TeV. The used data set has been recorded with the CMS detector and corresponds to an integrated luminosity of 2.3 fb^{-1}. In gauge-mediated supersymmetry breaking (GMSB) models the gauginos can decay to photons, or other standard model bosons, and gravitinos. The final state considered in this search is characterized by photons and missing transverse energy. Since in electroweak production scenarios the expected hadronic activity is low compared to strong production, no jet requirements are used. Additionally, gluino pair production models are considered, where the analysis does not lose sensitivity in scenarios with compressed mass spectra. The observed data are in agreement with the standard model prediction and limits are set on different models of GMSB.

1 Introduction

Supersymmetry [1–7] (SUSY) offers a solution to the gauge hierarchy problem [8], in many models provides a dark matter candidate, and allows for the unification of gauge couplings at high energy. In SUSY models of gauge-mediated SUSY breaking (GMSB) [9–15] the gravitino ($\widetilde{\mathrm{G}}$) is the lightest SUSY particle (LSP). If R-parity [16, 17] is conserved, SUSY particles are always produced in pairs and the gravitino LSP is stable so that it escapes undetected, leading to missing transverse energy ($E_{\mathrm{T}}^{\mathrm{miss}}$) in the detector. In the models considered here the gravitino is assumed to be essentially massless, ensuring prompt decays of the next-to-lightest SUSY particle (NLSP), which in all scenarios studied in this search is the lightest neutralino ($\widetilde{\chi}_1^0$). Depending on its composition, the $\widetilde{\chi}_1^0$ can decay according to $\widetilde{\chi}_1^0 \to \mathrm{N}\widetilde{\mathrm{G}}$, where N is either a photon γ, a SM Higgs boson H, or a Z boson. For $\widetilde{\chi}_1^0$ with a large bino component (bino-like $\widetilde{\chi}_1^0$), decays to photons are preferred. If the gauginos are nearly mass-degenerate, chargino ($\widetilde{\chi}_1^\pm$) decays like $\widetilde{\chi}_1^\pm \to \mathrm{W}^\pm\widetilde{\mathrm{G}}$ are also possible. An example Feynman graph of chargino-neutralino production with the typical decay of a bino-like $\widetilde{\chi}_1^0$ is shown in Fig. 1. Here, the $\widetilde{\chi}_2^0$ and $\widetilde{\chi}_1^\pm$ are considered to be wino-like. In scenarios with a small mass splitting between wino and bino, the decays of the $\widetilde{\chi}_2^0$ and $\widetilde{\chi}_1^\pm$ to the $\widetilde{\chi}_1^0$ plus SM boson are soft, leading to only a small contribution to the hadronic activity in the event.

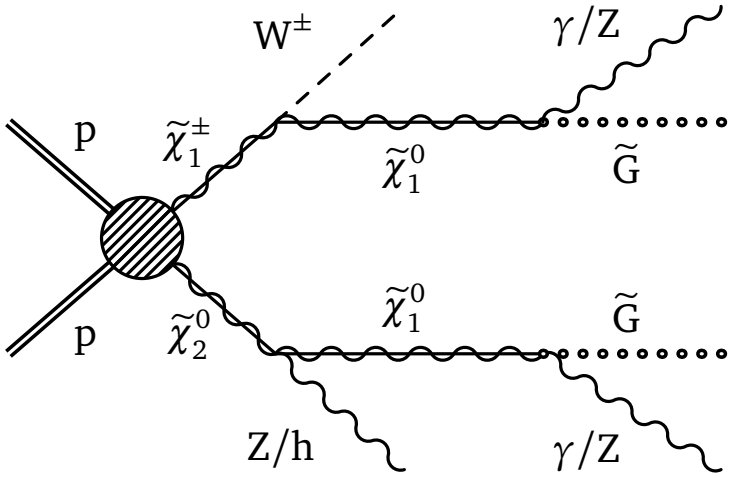

Figure 1: Feynman diagram of the dominant $\widetilde{\chi}_1^\pm$-$\widetilde{\chi}_2^0$ production mechanism and a typical decay chain in scenarios with a bino-like $\widetilde{\chi}_1^0$ and wino-like $\widetilde{\chi}_2^0$ and $\widetilde{\chi}_1^\pm$.

The analysis selects events with at least one photon and significant $E_{\mathrm{T}}^{\mathrm{miss}}$, mainly targeting electroweak production of supersymmetric particles in the context of GMSB scenarios, where hadronic energy arises only from initial-state radiation or from the decays of a $\mathrm{W}^\pm$ or Z boson, collectively denoted as V bosons. The mixing of the neutralino NLSP determines the final state. Bino- or wino-like mixing scenarios lead to final states with $E_{\mathrm{T}}^{\mathrm{miss}}$ and $\gamma\gamma$, Vγ, or VV. For bino-like mixtures, photon final states are most likely. A general gauge mediation (GGM) [18–23] scenario is used to guide the design of the analysis, where the $\widetilde{\chi}_1^0$ is assumed to be a pure bino, while the $\widetilde{\chi}_2^0$ and $\widetilde{\chi}_1^\pm$ are pure wino. Therefore, the neutralino and chargino masses are given by the bino and wino masses, $m_{\widetilde{\chi}_1^0} = m_{\widetilde{\mathrm{B}}}$ and $m_{\widetilde{\chi}_2^0} = m_{\widetilde{\chi}_1^\pm} = m_{\widetilde{\mathrm{W}}}$. Squarks and gluinos are decoupled, leading to electroweak production processes as shown in Fig. 1. The results of the search are also interpreted in the context of different simplified models. A simplified model called TChiWg of electroweak chargino-neutralino production with $\widetilde{\chi}_1^\pm \to \mathrm{W}^\pm\widetilde{\mathrm{G}}$ and $\widetilde{\chi}_1^0 \to \gamma\widetilde{\mathrm{G}}$ is shown in Fig. 2. Simplified models with gluino pair production are also considered. The gluinos $\widetilde{\mathrm{g}}$ decay to $\widetilde{\chi}_1^0$ or $\widetilde{\chi}_1^\pm$ and jets with subsequent decays $\widetilde{\chi}_1^0 \to \gamma\widetilde{\mathrm{G}}$ and $\widetilde{\chi}_1^\pm \to \mathrm{W}^\pm\widetilde{\mathrm{G}}$.

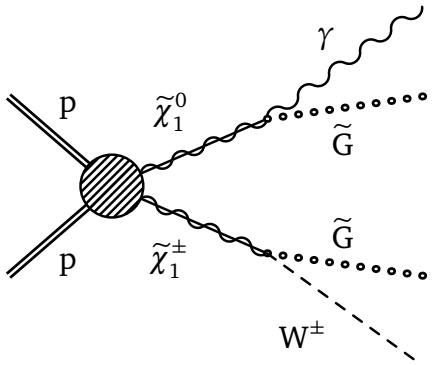

Figure 2: Feynman diagram corresponding to the TChiWg simplified model.

Other analyses specifically targeted at those models typically require jets in addition to photons. Though, in scenarios with compressed mass spectra the jets from the gluino decay are not reconstructed, which makes those analyses insensitive. Because no jet requirements are imposed in this analysis, there is no sensitivity loss for small $\Delta m(\widetilde{g}, \widetilde{\chi}_1^0/\widetilde{\chi}_1^\pm)$. The models are labeled according to the final state with two photons (T5gg) or a photon and a W boson (T5Wg). Feynman graphs for both models can be found in Fig. 3.

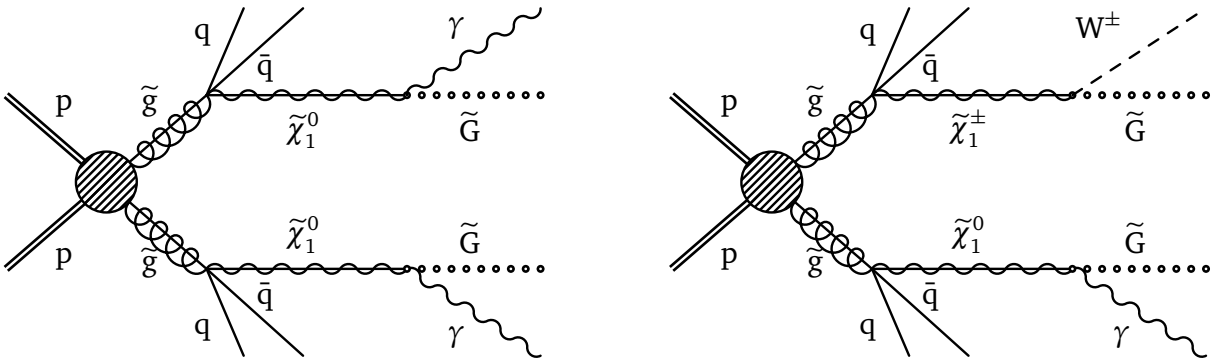

Figure 3: Feynman diagrams of the T5gg (left) and T5Wg (right) simplified models.

The analysis has been carried out before on data collected at a center-of-mass energy of 8 TeV at CMS [24]. A special "parked data set" [25] corresponding to an integrated luminosity of 7.4 fb^{-1} recorded with a photon+$E_{\text{T}}^{\text{miss}}$ trigger with low thresholds was used, whereas in this analysis a simple photon trigger is used.

In this search a proton-proton collision data set recorded in 2015 at a center-of-mass energy of 13 TeV is analyzed, which corresponds to an integrated luminosity of 2.3 fb^{-1}.

2 The CMS detector

The central feature of the CMS apparatus is a superconducting solenoid of 6 m internal diameter, providing a magnetic field of 3.8 T. Within the superconducting solenoid volume are a silicon pixel and strip tracker, a lead tungstate crystal electromagnetic calorimeter (ECAL), and a brass and scintillator hadron calorimeter (HCAL), each composed of a barrel and two endcap sections. Calorimeters and endcap detectors extend the pseudorapidity coverage of the barrel into the forward region [26]. Muons are measured in gas-ionization detectors embedded in the steel flux-return yoke outside the solenoid.

The particle-flow (PF) event algorithm reconstructs and identifies each individual particle with

an optimized combination of information from the various elements of the CMS detector. The energy of photons is directly obtained from the ECAL measurement, corrected for zero-suppression effects. The energy of electrons is determined from a combination of the electron momentum at the primary interaction vertex as determined by the tracker, the energy of the corresponding ECAL cluster, and the energy sum of all bremsstrahlung photons spatially compatible with originating from the electron track. The energy of muons is obtained from the curvature of the corresponding track. The energy of charged hadrons is determined from a combination of their momentum measured in the tracker and the matching ECAL and HCAL energy deposits, corrected for zero-suppression effects and for the response function of the calorimeters to hadronic showers. Finally, the energy of neutral hadrons is obtained from the corresponding corrected ECAL and HCAL energy.

Jets are clustered from particles reconstructed by the PF algorithm using the anti-k_t clustering algorithm [27] with a distance parameter of 0.4. Jet momentum is determined as the vectorial sum of all particle momenta in the jet, and is found from simulation to be within 5 to 10% of the true momentum over the whole p_{T} spectrum and detector acceptance. An offset correction is applied to jet energies to take into account the contribution from additional proton-proton interactions within the same or nearby bunch crossings. Jet energy corrections are derived from simulation, and are confirmed with in situ measurements of the energy balance in dijet and photon + jet events. Additional selection criteria are applied to each event to remove spurious jet-like features originating from isolated noise patterns in certain HCAL regions.

A more detailed description of the CMS detector, together with a definition of the coordinate system used and the relevant kinematic variables, can be found in Ref. [26].

3 Event selection

The data are recorded with a trigger requiring at least one photon with a p_{T} threshold of 165 GeV. In the offline analysis, an event is required to contain at least one well reconstructed vertex whose position is within 24 cm in z-direction around the nominal interaction point. Data quality filters are applied to reject events with anomalous signals from detector noise or contributions from beam halo. Only photons reconstructed in the barrel part ($|\eta| < 1.4442$) of the ECAL with $p_{\mathrm{T}} > 15$ GeV are considered, since the photons from NLSP decays are expected to be central. They are required to pass the standard identification criteria [28]. They have to be isolated from other energy deposits and need to have an ECAL cluster shape consistent with the expectation. The fraction of energy deposited in the HCAL tower closest to the cluster seed in the ECAL to the energy deposited in the ECAL has to be smaller than 5%. In addition, photons need to have a non-zero shower width in the ECAL to veto spontaneous discharges of the ECAL avalanche photodiodes. To distinguish photons from electrons, photon candidates are required to have no hits in the pixel detector that can be used to fit a track to the energy cluster in the ECAL. Finally, the photon (γ_1) with the largest transverse momentum in an event has to be separated from the nearest jet by $\Delta R > 0.5$, with $\Delta R = \sqrt{\Delta\phi^2 + \Delta\eta^2}$. Jets are required to have a minimum transverse momentum of 30 GeV and to be reconstructed within $|\eta| < 3.0$. For the identification of jets from b-quarks, b-tagging is performed using the Combined Secondary Vertex algorithm [29, 30]. The chosen tight working point corresponds to a b-tagging efficiency of $\varepsilon_{\mathrm{b}} \approx 49\%$ and a misidentification rate of $\approx 0.1\%$.

In order to be selected, an event is required to contain at least one photon with $p_{\mathrm{T}} > 180$ GeV that has been accepted by the trigger. In this region the trigger reaches a plateau efficiency of $97.5^{+0.9}_{-1.2}\%$. The uncertainty corresponds to a 68% CL Clopper-Pearson interval [31]. All simulated samples are scaled by this factor.

The analysis relies on the three kinematic variables $\mathcal{S}$, M_T, and S_T^γ defined below. To discriminate genuine $E_\mathrm{T}^\mathrm{miss}$ from instrumental $E_\mathrm{T}^\mathrm{miss}$, the $E_\mathrm{T}^\mathrm{miss}$ significance $\mathcal{S}$ [32, 33] is used, which is defined as a likelihood ratio

$$\mathcal{S} := 2 \ln \frac{\mathcal{L}(\vec{\varepsilon} = \vec{\varepsilon}_\mathrm{m})}{\mathcal{L}(\vec{\varepsilon} = 0)}$$

with the true $\vec{\varepsilon}$ and measured $\vec{\varepsilon}_\mathrm{m}$ missing transverse energy. The transverse mass M_T of the leading photon and the missing transverse energy is defined by

$$M_\mathrm{T}^2 = M_\mathrm{T}^2(\gamma_1, E_\mathrm{T}^\mathrm{miss}) := 2E_\mathrm{T}^\mathrm{miss} p_\mathrm{T}(\gamma_1) \left[1 - \cos\Delta\phi\left(E_\mathrm{T}^\mathrm{miss}, \gamma_1\right)\right] .$$

The events passing the preselection, $p_\mathrm{T}(\gamma_1) > 180\,\mathrm{GeV}$, are further categorized into a *signal region* (SR) and a *control region* (CR). The signal region is defined by $\mathcal{S} > 80$ and $M_\mathrm{T} > 300\,\mathrm{GeV}$, because for signal processes, a significant missing transverse energy is expected resulting from two LSPs escaping the detector undetected. In an event where only a single NLSP$\rightarrow \gamma$+LSP decay occured, $M_\mathrm{T}(\gamma_1, E_\mathrm{T}^\mathrm{miss})$ would correspond to the transverse mass of the NLSP. This is smeared by the second LSP emerging in the event, resulting in generally large values of M_T, because the NLSP is generally heavier than SM particles. The control region mainly used for the background estimation is defined as a side band to the SR by requiring $\mathcal{S} > 30$, $M_\mathrm{T} > 100\,\mathrm{GeV}$, and excluding the SR.

The variable S_T^γ is the sum of $E_\mathrm{T}^\mathrm{miss}$ and the transverse energy deposited by all photons,

$$S_\mathrm{T}^\gamma := E_\mathrm{T}^\mathrm{miss} + \sum_\mathrm{photons} p_\mathrm{T} .$$

Owing to the good signal sensitivity, the S_T^γ distribution in the signal region is used for the final interpretation of the search. Since the part with $S_\mathrm{T}^\gamma < 600\,\mathrm{GeV}$ is not signal-sensitive, it is excluded from the SR and used as a validation region (VR) for the background prediction. The three regions (SR, CR, VR) are sketched in Fig. 4.

4 Event simulation and background estimation

The dominant SM backgrounds for this search are the production of $\mathrm{W}(\rightarrow \ell\nu)$ and $\mathrm{Z}(\rightarrow \nu\nu)$ in association with a photon, in the following denoted V+γ, due to the neutrino(s) which result in missing transverse energy.

A further background with a large contribution especially in the control region selection comes from multijet events, where either a jet is misreconstructed as a photon (QCD multijet) or a real photon is radiated (γ+jets), the latter having the larger contribution. Although such events are balanced at parton level, missing transverse energy arises from the limited detector resolution, especially of the HCAL. This background is important because of its large cross section. The $\mathrm{V}(+\gamma)$ and $(\gamma+)$jets backgrounds are estimated starting from simulated samples. These samples are then scaled by correction factors which are derived simultaneously using a template fit to the data in the control region.

Further smaller, but non-negligible backgrounds are events containing electrons that are misidentified as photons ($\mathrm{e} \rightarrow \gamma$) and $\mathrm{t\bar{t}}$ events with photon radiation. For the estimation of the $\mathrm{e} \rightarrow \gamma$ background a common data driven approach is used. $\mathrm{t\bar{t}}$ events with photon radiation ($\mathrm{t\bar{t}} + \gamma$), as well as the remaining contributions of $\mathrm{t\bar{t}}$ and diboson production (WW, WZ, ZZ) due to jets misreconstructed as photons are determined completely from simulation.

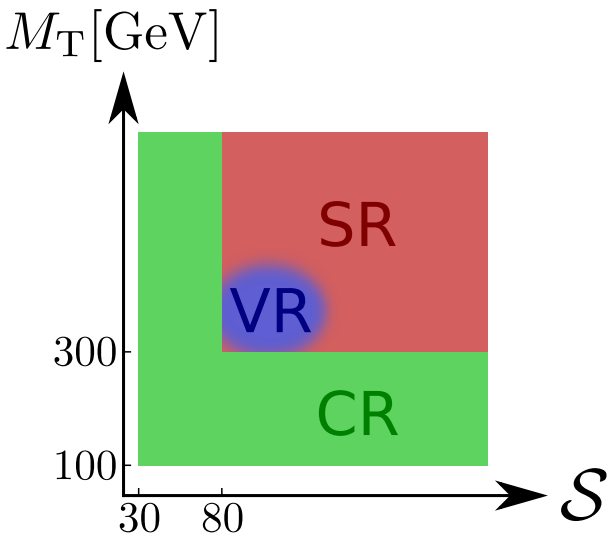

Figure 4: Sketch of the control (CR) and signal region (SR) definitions. The validation region (VR) is not defined in the $\mathcal{S}$-M_{T} plane, but embedded in the SR with the additional condition $S_{\mathrm{T}}^{\gamma} < 600\,\mathrm{GeV}$. This corresponds approximately to the bottom-left corner of the SR, which is therefore illustrated as a blurred region.

QCD multijet and γ+jets events, as well as the $\mathrm{Z/W}(+\gamma)$, ZZ, and WZ samples are generated with MADGRAPH [34] in leading order (LO) in α_s, while the $\mathrm{t\bar{t}}(+\gamma)$ processes are generated with MADGRAPH MC@NLO. For WW production, the POWHEG generator is used [35–39]. The fragmentation and hadronization are handled with PYTHIA 8 [40, 41] and the detector response is modeled with GEANT4 [42]. All generated samples are weighted on an event-by-event basis to match the number of primary interactions per bunch crossing (pileup) to the data.

Backgrounds taken from simulation are corrected with the highest order correction factors available. The $\mathrm{Z}+\gamma$ sample is corrected with photon p_{T} dependent next-to-next-to-leading-order (NNLO) k-factors and a constant NNLO k-factor is applied for $\mathrm{W}+\gamma$ [43]. For the W and $\mathrm{Z}(\to \nu\nu)$ simulation constant next-to-leading-order (NLO) k-factors are used. Cross sections for diboson processes are available in NLO (ZZ, WZ) and NNLO (WW) [44].

Figure 5 shows the $\mathcal{S}$ and M_{T} distributions after the preselection (photon $p_{\mathrm{T}} > 180\,\mathrm{GeV}$). In these plots the $\mathrm{e} \to \gamma$ background is determined using the data-driven method explained in Section 4.2, while all other backgrounds are taken from simulation as described above. Three signal mass points are shown, namely

- GGM: $m_{\widetilde{\mathrm{W}}} = 640\,\mathrm{GeV}$, $m_{\widetilde{\mathrm{B}}} = 630\,\mathrm{GeV}$,
- T5gg: $m_{\widetilde{\mathrm{g}}} = 1400\,\mathrm{GeV}$, $m_{\widetilde{\chi}_1^0} = 1200\,\mathrm{GeV}$, and
- T5Wg: $m_{\widetilde{\mathrm{g}}} = 1550\,\mathrm{GeV}$, $m_{\widetilde{\chi}_1^0} = 1500\,\mathrm{GeV}$.

All T5gg, T5Wg, and TChiWg samples are generated using LO MADGRAPH [34] simulation and NLO cross sections for the production are used [45–47]. GGM signal is simulated using PYTHIA 8 [40, 41] and NLO cross sections are calculated using Prospino [48].

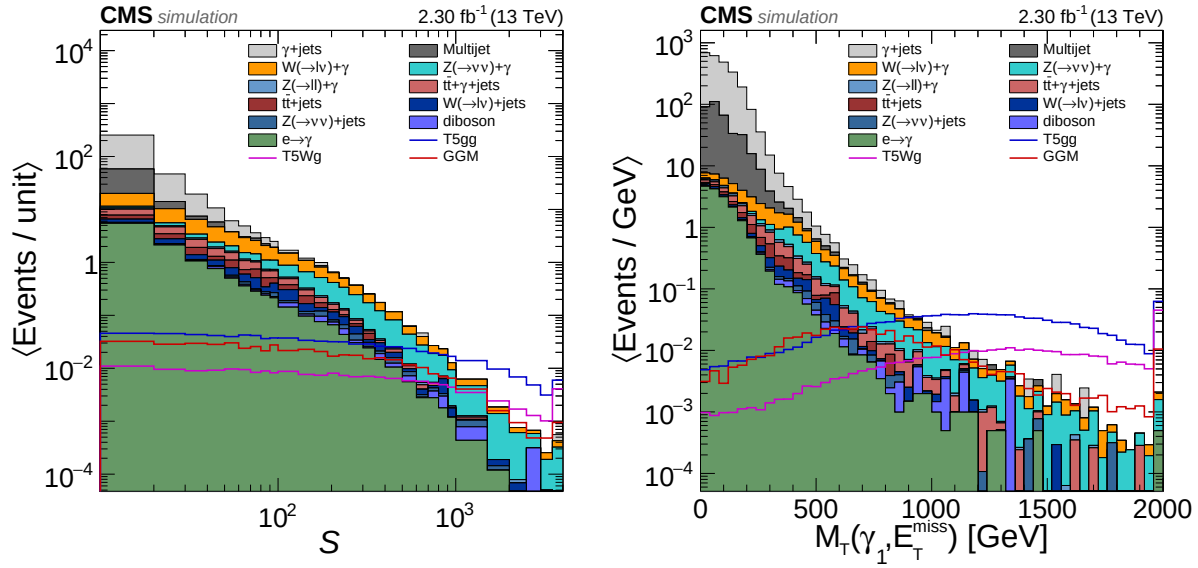

Figure 5: The $\mathcal{S}$ and M_{T} distributions after the preselection. The overflow is contained in the last bin shown and the bin contents are divided by the bin widths.

4.1 Main backgrounds: W/Z$(+\gamma)$ and $(\gamma+)$jets

For the dominant backgrounds, scale factors are derived in the signal depleted control region using a template fit, i.e. template distributions for different backgrounds are taken from simulation and the normalization of the single templates is scaled to match the distribution observed in data. For this purpose, the simulated background samples are grouped into

- $(\gamma+)$jets = {Multijet, $\gamma+$jets},
- V$(+\gamma)$ = {W$(+\gamma)$, Z$(+\gamma)$},
- fixed = {$\mathrm{t\bar{t}}(+\gamma)$, e $\rightarrow \gamma$, diboson} .

The normalization of each of the first two categories is determined by the fit, while the fixed backgrounds cannot vary. To minimize the influence of $\mathrm{t\bar{t}}(+\gamma)$, which is the main part of the fixed backgrounds, the fit is performed in the CR with the additional requirement that no jet in an event is b-tagged.

To be able to reliably determine both normalizations, the variable used for the template distributions has to separate the single background components. The variable used for the fit is $|\Delta\phi|(E_{\mathrm{T}}^{\mathrm{miss}}, \mathrm{jet}_1)$, because in this distribution the main backgrounds $(\gamma+)$jets and V$(+\gamma)$ have different shapes as can be seen in Fig. 6. For $(\gamma+)$jets, the missing transverse energy tends to be aligned with a jet, because of jet energy mismeasurements, which in most cases is the leading jet (jet_1). Compared to the resulting concentration of $|\Delta\phi|(E_{\mathrm{T}}^{\mathrm{miss}}, \mathrm{jet}_1)$ at low values, the V$(+\gamma)$ events show a uniform distribution.

An extended maximum likelihood fit is performed where the normalizations N_i^{fit} ($i \in \{(\gamma+)\mathrm{jets}, \mathrm{V}(+\gamma)\}$) are free parameters. Scale factors

$$\mathrm{SF}_i = N_i^{\mathrm{fit}} / N_i^{\mathrm{init}}$$

are derived from the initial number N_i^{init} of events contained in template i and the number N_i^{fit} determined by the fit. The results of the fit are

$$\mathrm{SF}_{(\gamma+)\mathrm{jets}} = 1.46 \pm 0.13, \tag{1a}$$

$$\mathrm{SF}_{\mathrm{V}(+\gamma)} = 0.69 \pm 0.17, \tag{1b}$$

and are shown in Fig. 6. The uncertainties of the fit are of statistical origin and the corresponding correlation is $\rho = -0.64$. For the LO (γ+)jets template a scale factor larger than unity is expected owing to missing higher order corrections in α_s that would increase the cross section. The V(+γ) template is already corrected with QCD NNLO *k*-factors. Additional electroweak corrections are expected to decrease the cross section, which explains a scale factor lower than unity. The total post-fit distribution shows a good agreement with the data.

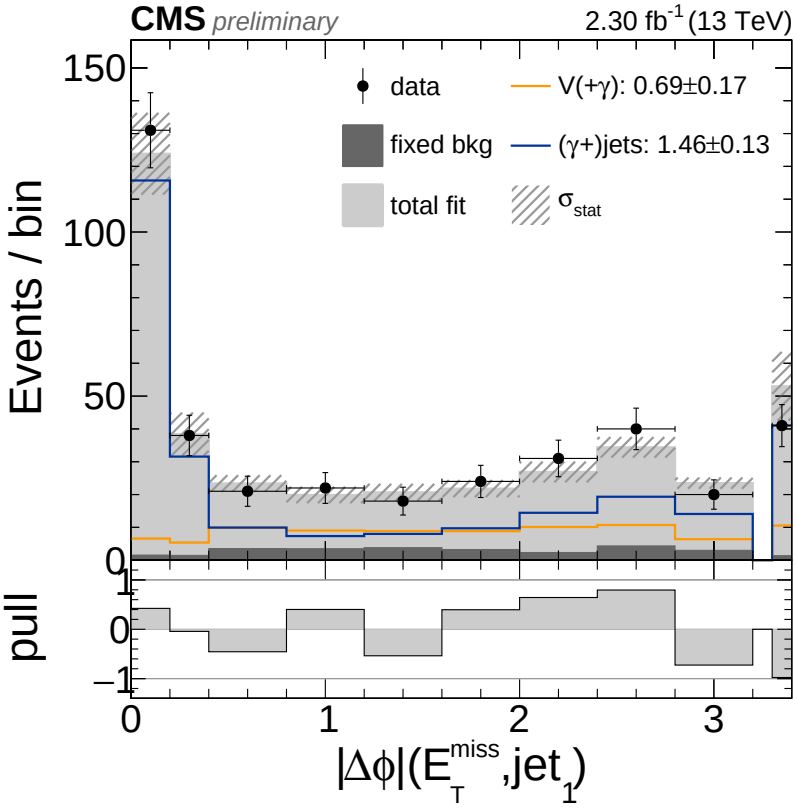

Figure 6: Template fit result: The post-fit distributions for (γ+)jets and V(+γ) together with the total fit distribution stacked onto the fixed backgrounds. Events containing zero jets are counted in the last shown bin. The values in the legend are the resulting scale factors.

The obtained scale factors are applied to the corresponding simulated samples to predict the (γ+)jets and V(+γ) backgrounds in the signal region.

All main uncertainties of the simulation that correspond to a normalization uncertainty are eliminated by this MC normalization method. The remaining uncertainty is the uncertainty of the fit parameters due to the limited statistical precision of the used samples. A variation in the renormalization and factorization scales was found to have no significant influence on the V(+γ) template, whereas a variation of up to 13% was found for the (γ+)jets scale factor. This is considered as a separate systematic uncertainty. It has been verified that possible uncertainties due to shape variations and higher order corrections are negligible compared to the fit uncertainty. The method has been tested on simulated toy data for different contribution strengths of the individual background components to ensure that no bias of the fit result is introduced. The statistical fit errors are considered as a systematic uncertainty for the prediction of the main backgrounds. For the final interpretation of the search results, the anti-correlation of these is taken into account.

4.2 Background from electrons misidentified as photons

To estimate the contribution of electrons misidentified as photons, a data driven tag-and-probe approach is used. The tag object is a well reconstructed electron, defined like a photon but requiring a pixel seed (γ_{pix}). The probe is an object fulfilling the photon identification criteria, but which is not checked for a pixel seed. To get a large fraction of real electrons in the probe sample, $Z \to ee$ events are selected. The invariant mass of the tag and probe objects is required to be consistent with the Z boson mass. After the subtraction of non-Z backgrounds, the number of events in which the probe object does pass the pixel seed veto is used to determine the misidentification rate f. The value determined in data is $f = 1.94\%$ and an uncertainty of 30% is estimated based on the variation of the value as a function of photon p_{T} and η. To determine the $e \to \gamma$ background, the event selection is repeated, but selecting γ_{pix} instead of photons. The resulting distribution is finally scaled by the transfer factor $R = f/(1-f)$. To avoid double counting of $e \to \gamma$ events, all simulated events where the reconstructed leading photon can be matched to a generated electron are rejected.

5 Systematic uncertainties

The relative systematic uncertainties are listed in Table 1. The uncertainties resulting from the statistical precision of the fit are considered with the corresponding correlation coefficient. For the other less relevant backgrounds that are taken from simulation, sources of systematic uncertainty are cross section, PDF and scale uncertainties. The latest cross section measurements for $t\bar{t}(+\gamma)$ [49] and diboson production [50–52] are covered by an uncertainty of 30% and 20%, respectively. For the backgrounds and signals that are taken from simulation, the uncertainties of the trigger efficiency (1%) and the luminosity (2.3%) are considered fully correlated. An additional uncertainty of 1% is included that covers possible differences in the photon identification efficiency in data and simulation. Differences in the jet misidentification rate are found to be negligible in this analysis. The total background uncertainty is dominated by the uncertainty of the $V(+\gamma)$ background prediction.

Table 1: Systematic uncertainties of the separate backgrounds. The uncertainties are relative to the respective backgrounds.

	$V(+\gamma)$	$(\gamma+)$jets	$e \to \gamma$	$t\bar{t}(+\gamma)$	Diboson	Signal
Fit uncert. of statistical origin	25%	9%	-	-	-	-
Scale uncert. influence on fit	-	13%	-	-	-	-
Tag-and-Probe fit	-	-	30%	-	-	-
MC statistical precision	$1-3\%$	$21-27\%$	-	$14-25\%$	$47-66\%$	$2-10\%$
Cross section, PDF, scale	-	-	-	30%	20%	-
Luminosity	-	-	-	2.3%	2.3%	2.3%
Trigger efficiency	-	-	-	1%	1%	1%
Photon ID	-	-	-	1%	1%	1%

6 Validation of the background prediction

The total background prediction is tested in the control region for several different distributions. A comparison of the prediction to data for the main observables $\mathcal{S}$, M_{T}, and S_{T}^{γ}, as well as for photon p_{T}, can be seen in Fig. 7. Overall, a good description of the data is observed.

To further validate the obtained scale factor for $V(+\gamma)$, a $W + \gamma$ enriched subset of the CR is

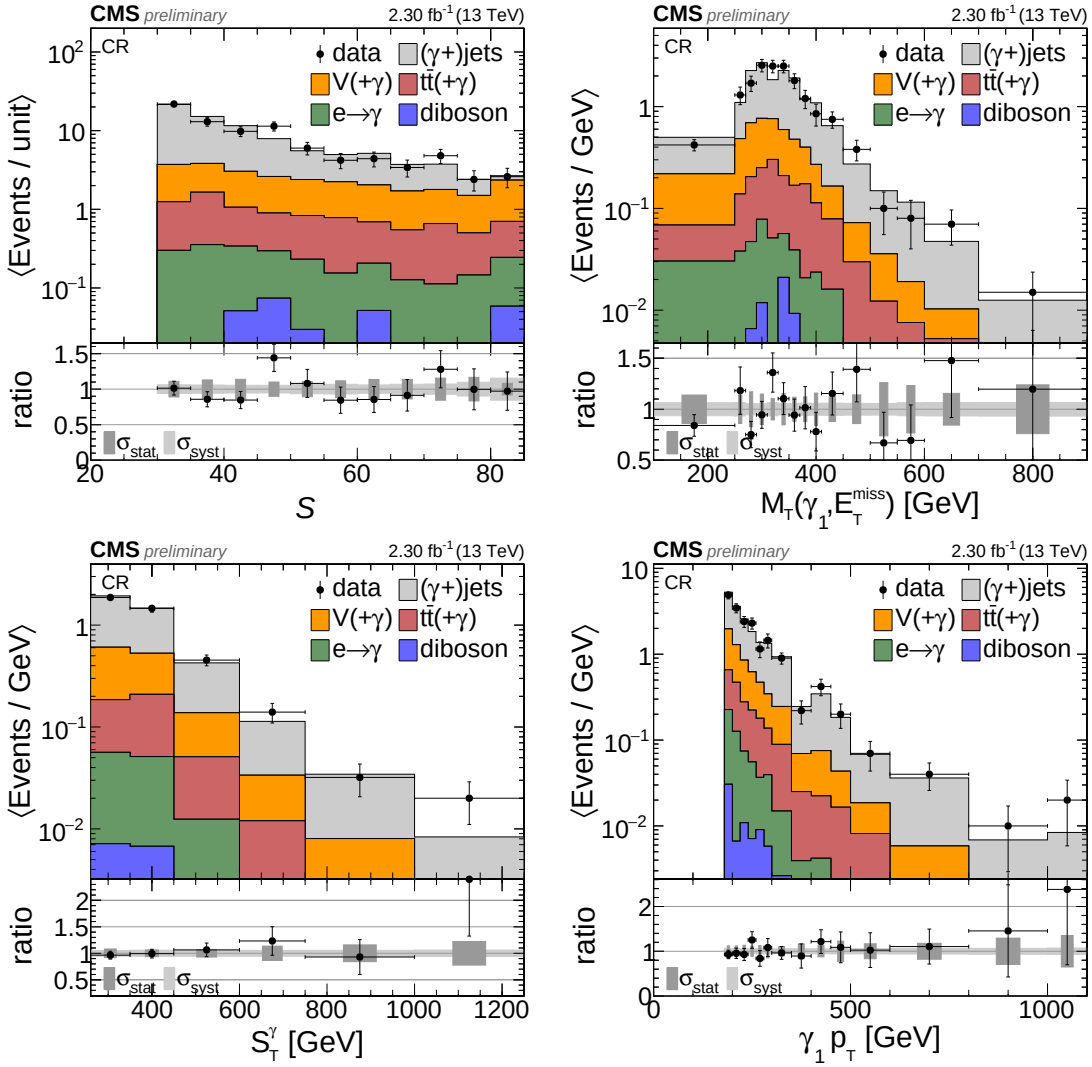

Figure 7: Comparison of the total background prediction to data in the control region without a b-jet veto. Top: $E_{\mathrm{T}}^{\mathrm{miss}}$ significance (left) and transverse mass (right). Bottom: S_{T}^{γ} (left) and leading photon p_{T} (right). The overflow is contained in the last bin. The bin contents are divided by the bin widths.

selected by requiring the presence of exactly one isolated electron or muon. Figure 8 shows that the normalization using the scale factor given in Eq. (1) fits well also for this subset of the data.

Finally, it is verified that the background prediction still describes the data distributions when extrapolating the scale factors from the CR and applying them in the dedicated validation region. The predicted background together with data is shown in Fig. 9. The normalization agrees within the uncertainties and also the shapes of the important observables are reasonably well modeled.

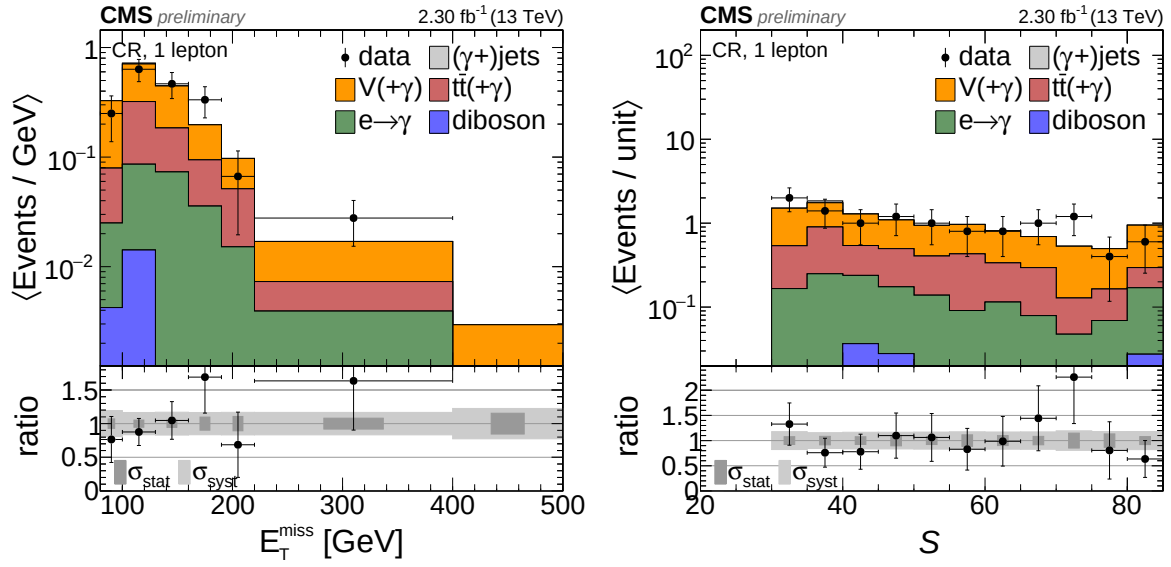

Figure 8: Comparison of the total background prediction to data in the control region with the additional requirement of exactly one lepton. Left: missing transverse energy. Right: $E_{\mathrm{T}}^{\mathrm{miss}}$ significance. The overflow is contained in the last bin. The bin contents are divided by the bin widths.

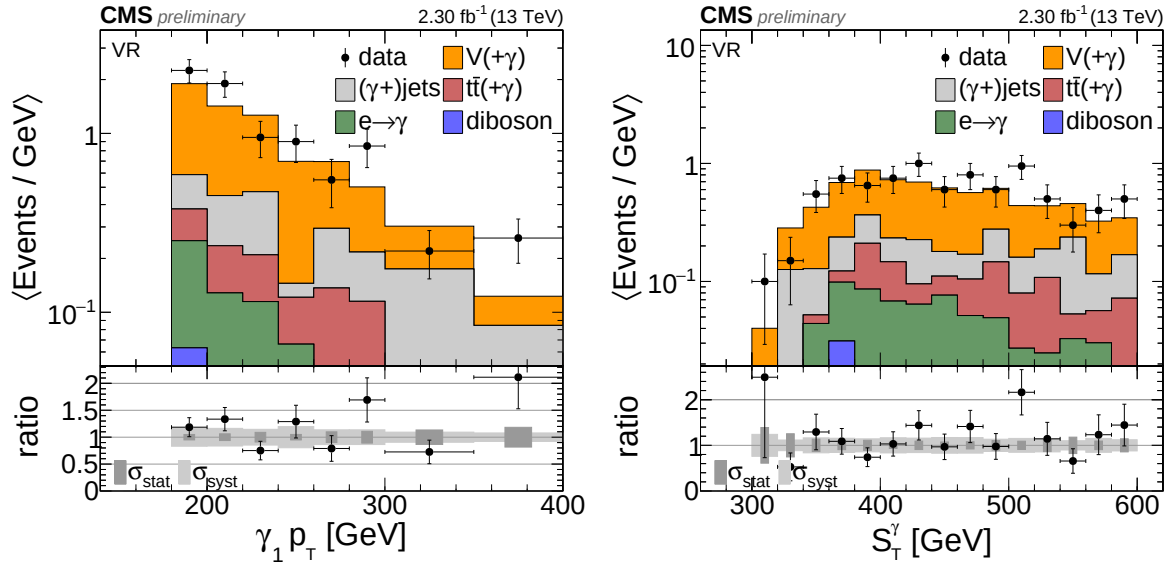

Figure 9: Comparison of the total background prediction to data in the validation region. Left: leading photon p_{T}. Right: S_{T}^{γ}. The overflow is contained in the last bin. The bin contents are divided by the bin widths.

7 Results

The signal region is divided into three exclusive bins in S_T^γ. These are shown in Fig. 10 for the total background prediction and the data. All three example signal points shown in previous plots are also included here. Background and signal histograms are stacked to visualize the possible influence of signal presence. The data is found to be in agreement with the SM prediction and no sign of SUSY is found. Additionally, the yields for the separate bins can be found in Table 2. The contributions of the individual background components are listed in Table 3 together with the corresponding uncertainties. The systematic uncertainties of the single background components are combined, taking the correlation term for $V(+\gamma)$ and $(\gamma+)$jets into account.

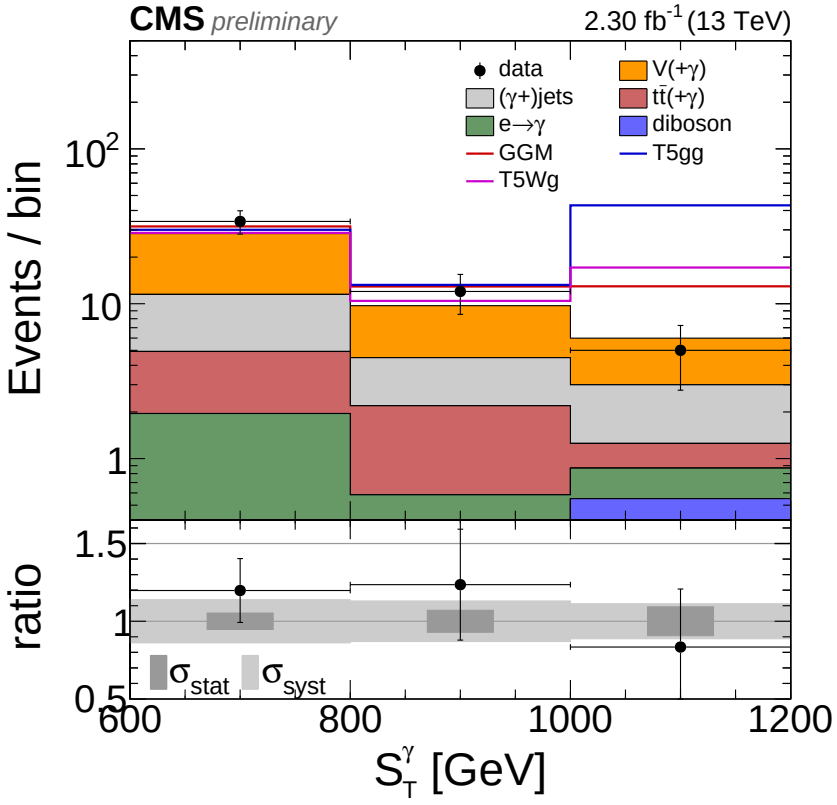

Figure 10: Background and data distributions in the signal region using the final binning in S_T^γ. The last bin contains the overflow. The background and signal histograms are stacked.

Table 2: Yields for the individual SR bins. For the total systematic uncertainties the correlation term for the systematic uncertainties of $V(+\gamma)$ and $(\gamma+)$jets has been considered.

S_T^γ[GeV]	prediction	σ_{stat}	σ_{syst}	data
$600-800$	28.4	±1.5	±4.1	34
$800-1000$	9.7	±0.7	±1.3	12
$1000-\infty$	6.0	±0.6	±0.7	5

No evidence for physics beyond the standard model is found and limits are calculated to constrain the allowed parameter space of different models. The focus is on models of electroweak production. Additionally, two gluino pair production models are considered.

Upper limits on the cross section are calculated for the different models at 95% confidence level (CL) using a frequentist CL_s approach [53–55] with a profile likelihood test statistic and

Table 3: Individual background yields for the separate signal region bins. The statistical uncertainty of the e $\to \gamma$ background is due to the limited size of the collected data sample. All other statistical uncertainties are due to the limited number of simulated events.

	S_T^γ bin: 600 − 800 GeV			S_T^γ bin: 800 − 1000 GeV			S_T^γ bin: 1000 − ∞ GeV		
	yield	σ_{stat}	σ_{syst}	yield	σ_{stat}	σ_{syst}	yield	σ_{stat}	σ_{syst}
$V(+\gamma)$	16.90	0.27	4.16	5.23	0.12	1.29	3.00	0.09	0.74
$(\gamma+)$jets	6.57	1.40	1.03	2.29	0.56	0.36	1.74	0.47	0.27
$t\bar{t}(+\gamma)$	2.96	0.41	0.89	1.61	0.34	0.48	0.39	0.09	0.12
e $\to \gamma$	1.62	0.18	0.49	0.36	0.08	0.11	0.32	0.08	0.09
diboson	0.33	0.16	0.07	0.23	0.15	0.05	0.55	0.26	0.11

asymptotic formulae [56]. The limits for the GGM model are shown in Fig. 11 for the individual mass points. A point with a cross section larger than the calculated limit can be excluded. The exclusion contour in the bino-wino ($m_{\tilde{B}} - m_{\tilde{W}}$) mass plane is shown. Additionally, an expected limit contour is included, reflecting the expectation for data distributed according to the SM prediction. The observed limit contour is weaker than the expected at lower NLSP masses, because these correspond to lower photon p_T and E_T^{miss}. Therefore, the first two signal region bins which show slight overfluctuations have a larger influence. For larger masses, the last SR bin is more important. Here, a small underfluctuation is observed, resulting in the observed limit getting stronger. The limit for the TChiWg model is shown as a function of the single mass parameter m_{NLSP} in Fig. 12 together with the theoretical cross section. NLSP masses below approximately 450 GeV can be excluded. For the electroweak production models the limits of the 8 TeV search cannot be improved, since the rise in cross section for $\sqrt{s}$ moving from 8 TeV to 13 TeV is not as large as for strong production scenarios. It is expected that the sensitivity will be greatly increased with more data collected at $\sqrt{s} = 13$ TeV.

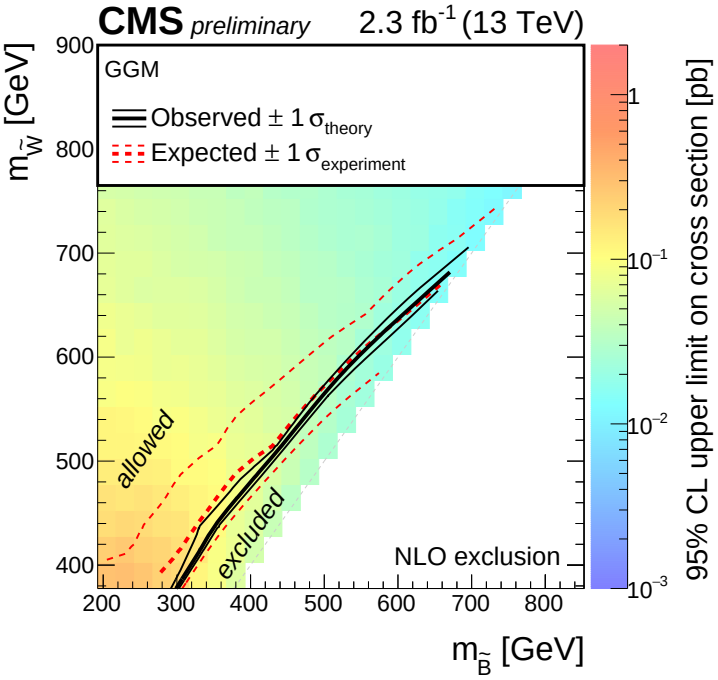

Figure 11: The 95% CL limits for the GGM model in the bino-wino mass plane. The color scale encodes the observed upper cross section limit for each point. The lines represent the observed (black) and expected (red) exclusion contours and their uncertainties.

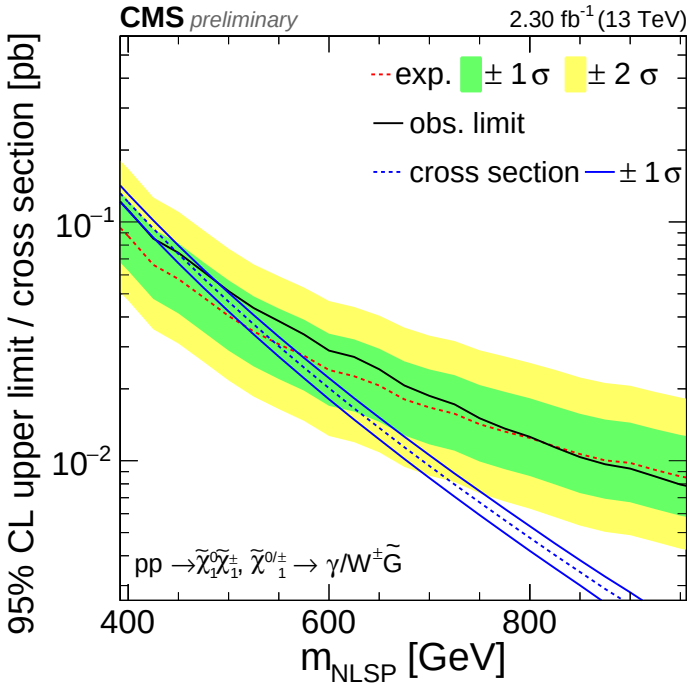

Figure 12: Observed and expected upper cross section limits as a function of the NLSP mass for the TChiWg model together with the theoretical cross section.

Similar interpretations for the simplified models T5gg and T5Wg of gluino pair production are provided. The cross section limits and exclusion contours can be found in Figs. 13 and 14 in the $\tilde{g} - \tilde{\chi}_1^0/\tilde{\chi}_1^\pm$ mass plane. The currently strongest limit set by CMS for the T5gg model is provided by the search requiring two photons (using the same data set), excluding gluino masses below $\approx$ 1550 GeV for $m_{\tilde{\chi}_1^0} > 200$ GeV [57]. This search can exclude gluino masses of up to 1740 GeV at the diagonal. The limit gets weaker at low NSLP masses because of the acceptance loss, which is stronger than that of an analysis selecting two photons with lower p_T thresholds. The T5Wg exclusion contours generally exhibit the same shape, but with a slightly weaker exclusion power. The lower sensitivity is due to the fact that there is only one photon contributing to S_T^γ. Gluino masses of up to 1690 GeV can be excluded at the diagonal.

8 Summary

A search for the production of supersymmetric particles decaying to photons is presented. The data sample used corresponds to 2.3 fb^{-1} of pp collisions recorded with the CMS detector in 2015 at $\sqrt{s} = 13$ TeV. A cut-and-count experiment is performed in three exclusive search bins. The observed event counts are in agreement with the SM prediction. Exclusion limits at the 95% CL are set for a general gauge mediation model of electroweak production and the simplified model TChiWg. The limits for the electroweak production models cannot be improved with respect to the 8 TeV search. A much larger sensitivity is expected with more integrated luminosity collected at $\sqrt{s} = 13$ TeV.

Additionally, limits are set for two simplified models (T5gg, T5Wg) assuming gluino pair production. The currently best CMS limits are improved in regions with large NLSP masses.

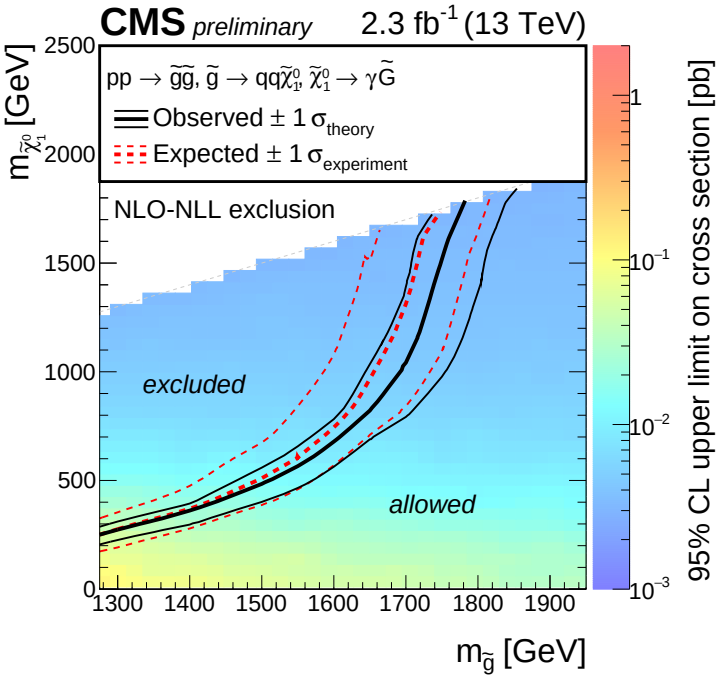

Figure 13: The 95% CL limits for the T5gg model in the gluino-neutralino mass plane. The color scale encodes the observed upper cross section limit for each point. The lines represent the observed (black) and expected (red) exclusion contours and their uncertainties.

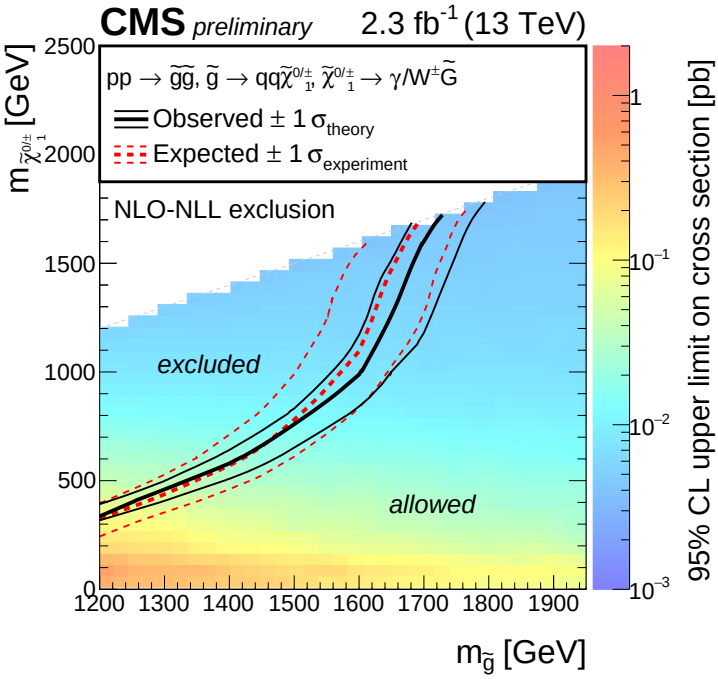

Figure 14: The 95% CL limits for the T5Wg model in the gluino-neutralino mass plane. The color scale encodes the observed upper cross section limit for each point. The lines represent the observed (black) and expected (red) exclusion contours and their uncertainties.

References

[1] P. Ramond, "Dual theory for free fermions", *Phys. Rev. D* **3** (1971) 2415, doi:10.1103/PhysRevD.3.2415.

[2] J. Wess and B. Zumino, "Supergauge transformations in four-dimensions", *Nucl. Phys. B* **70** (1974) 39, doi:10.1016/0550-3213(74)90355-1.

[3] D. Z. Freedman, P. van Nieuwenhuizen, and S. Ferrara, "Progress toward a theory of supergravity", *Phys. Rev. D* **13** (1976) 3214, doi:10.1103/PhysRevD.13.3214.

[4] P. Fayet, "Supergauge invariant extension of the Higgs mechanism and a model for the electron and its neutrino", *Nucl. Phys. B* **90** (1975) 104, doi:10.1016/0550-3213(75)90636-7.

[5] A. H. Chamseddine, R. L. Arnowitt, and P. Nath, "Locally supersymmetric grand unification", *Phys. Rev. Lett.* **49** (1982) 970, doi:10.1103/PhysRevLett.49.970.

[6] L. J. Hall, J. D. Lykken, and S. Weinberg, "Supergravity as the messenger of supersymmetry breaking", *Phys. Rev. D* **27** (1983) 2359, doi:10.1103/PhysRevD.27.2359.

[7] G. L. Kane, C. F. Kolda, L. Roszkowski, and J. D. Wells, "Study of constrained minimal supersymmetry", *Phys. Rev. D* **49** (1994) 6173, doi:10.1103/PhysRevD.49.6173, arXiv:hep-ph/9312272.

[8] R. Barbieri and G. F. Giudice, "Upper bounds on supersymmetric particle masses", *Nucl. Phys. B* **306** (1988) 63, doi:10.1016/0550-3213(88)90171-X.

[9] P. Fayet, "Mixing between gravitational and weak interactions through the massive gravitino", *Phys. Lett. B* **70** (1977) 461, doi:10.1016/0370-2693(77)90414-2.

[10] H. Baer, M. Brhlik, C. H. Chen, and X. Tata, "Signals for the minimal gauge-mediated supersymmetry breaking model at the Fermilab Tevatron collider", *Phys. Rev. D* **55** (1997) 4463, doi:10.1103/PhysRevD.55.4463, arXiv:hep-ph/9610358.

[11] H. Baer, P. G. Mercadante, X. Tata, and Y. L. Wang, "Reach of Tevatron upgrades in gauge-mediated supersymmetry breaking models", *Phys. Rev. D* **60** (1999) 055001, doi:10.1103/PhysRevD.60.055001, arXiv:hep-ph/9903333.

[12] S. Dimopoulos, S. Thomas, and J. D. Wells, "Sparticle spectroscopy and electroweak symmetry breaking with gauge-mediated supersymmetry breaking", *Nucl. Phys. B* **488** (1997) 39, doi:10.1016/S0550-3213(97)00030-8, arXiv:hep-ph/9609434.

[13] J. R. Ellis, J. L. Lopez, and D. V. Nanopoulos, "Analysis of LEP constraints on supersymmetric models with a light gravitino", *Phys. Lett. B* **394** (1997) 354, doi:10.1016/S0370-2693(97)00019-1, arXiv:hep-ph/9610470.

[14] M. Dine, A. E. Nelson, Y. Nir, and Y. Shirman, "New tools for low energy dynamical supersymmetry breaking", *Phys. Rev. D* **53** (1996) 2658, doi:10.1103/PhysRevD.53.2658, arXiv:hep-ph/9507378.

[15] G. F. Giudice and R. Rattazzi, "Gauge-mediated supersymmetry breaking", in *Perspectives on supersymmetry*, p. 355. World Scientific, Singapore, 1998.

[16] R. Barbier et al., "R-parity violating supersymmetry", *Phys.Rept.* **420** (2005) 1, arXiv:hep-ph/0406039.

[17] G. R. Farrar and P. Fayet, "Phenomenology of the production, decay, and detection of new hadronic states associated with supersymmetry", *Phys. Lett. B* **76** (1978) 575, doi:10.1016/0370-2693(78)90858-4.

[18] P. Meade, N. Seiberg, and D. Shih, "General gauge mediation", *Prog. Theor. Phys. Suppl.* **177** (2009) 143, doi:10.1143/PTPS.177.143, arXiv:0801.3278.

[19] M. Buican, P. Meade, N. Seiberg, and D. Shih, "Exploring general gauge mediation", *JHEP* **03** (2009) 016, doi:10.1088/1126-6708/2009/03/016, arXiv:0812.3668.

[20] J. T. Ruderman and D. Shih, "General neutralino NLSPs at the early LHC", *JHEP* **08** (2012) 159, doi:10.1007/JHEP08(2012)159, arXiv:1103.6083.

[21] Y. Kats, P. Meade, M. Reece, and D. Shih, "The status of GMSB after 1/fb at the LHC", *JHEP* **02** (2012) 115, doi:10.1007/JHEP02(2012)115, arXiv:1110.6444.

[22] Y. Kats and M. J. Strassler, "Probing colored particles with photons, leptons, and jets", *JHEP* **11** (2012) 097, doi:10.1007/JHEP11(2012)097, arXiv:1204.1119.

[23] P. Grajek, A. Mariotti, and D. Redigolo, "Phenomenology of general gauge mediation in light of a 125 GeV Higgs", *JHEP* **07** (2013) 109, doi:10.1007/JHEP07(2013)109, arXiv:1303.0870.

[24] CMS Collaboration, "Search for supersymmetry in electroweak production with photons and large missing transverse energy in pp collisions at $\sqrt{s}$ = 8 TeV", *Phys. Lett. B* **759** (2016) 479, doi:10.1016/j.physletb.2016.05.088, arXiv:1602.08772.

[25] CMS Collaboration, "Data parking and data scouting at the CMS experiment", CMS Performance note CMS-DP-2012-022, CERN, (2012).

[26] CMS Collaboration, "The CMS experiment at the CERN LHC", *JINST* **3** (2008) S08004, doi:10.1088/1748-0221/3/08/S08004.

[27] M. Cacciari, G. P. Salam, and G. Soyez, "The anti-k_t jet clustering algorithm", *JHEP* **04** (2008) 063, doi:10.1088/1126-6708/2008/04/063, arXiv:0802.1189.

[28] CMS Collaboration, "Performance of photon reconstruction and identification with the CMS detector in proton-proton collisions at $\sqrt{s} = 8$ TeV", *JINST* **10** (2015) P08010, doi:10.1088/1748-0221/10/08/P08010, arXiv:1502.02702.

[29] CMS Collaboration, "Identification of b-quark jets with the CMS experiment", *JINST* **8** (2013) P04013, doi:10.1088/1748-0221/8/04/P04013, arXiv:1211.4462.

[30] CMS Collaboration, "Identification of b quark jets at the CMS Experiment in the LHC Run 2", CMS Physics Analysis Summary CMS-PAS-BTV-15-001, CERN, Geneva, 2016.

[31] C. J. Clopper and E. S. Pearson, "The use of confidence or fiducial limits illustrated in the case of the binomial", *Biometrika* **26** (1934), no. 4, 404, doi:10.1093/biomet/26.4.404.

[32] CMS Collaboration, "Missing transverse energy performance of the CMS detector", *JINST* **6** (2011) P09001, doi:10.1088/1748-0221/6/09/P09001, arXiv:1106.5048.

[33] CMS Collaboration, "Performance of the CMS missing transverse momentum reconstruction in pp data at $\sqrt{s}$ = 8 TeV", *JINST* **10** (2015), no. 02, P02006, doi:10.1088/1748-0221/10/02/P02006, arXiv:1411.0511.

[34] J. Alwall et al., "The automated computation of tree-level and next-to-leading order differential cross sections, and their matching to parton shower simulations", *JHEP* **07** (2014) 079, doi:10.1007/JHEP07(2014)079, arXiv:1405.0301.

[35] P. Nason, "A New method for combining NLO QCD with shower Monte Carlo algorithms", *JHEP* **11** (2004) 040, doi:10.1088/1126-6708/2004/11/040, arXiv:hep-ph/0409146.

[36] S. Frixione, P. Nason, and C. Oleari, "Matching NLO QCD computations with Parton Shower simulations: the POWHEG method", *JHEP* **11** (2007) 070, doi:10.1088/1126-6708/2007/11/070, arXiv:0709.2092.

[37] S. Alioli, P. Nason, C. Oleari, and E. Re, "A general framework for implementing NLO calculations in shower Monte Carlo programs: the POWHEG BOX", *JHEP* **06** (2010) 043, doi:10.1007/JHEP06(2010)043, arXiv:1002.2581.

[38] T. Melia, P. Nason, R. Rontsch, and G. Zanderighi, "W+W-, WZ and ZZ production in the POWHEG BOX", *JHEP* **11** (2011) 078, doi:10.1007/JHEP11(2011)078, arXiv:1107.5051.

[39] P. Nason and G. Zanderighi, "W^+W^- , WZ and ZZ production in the POWHEG-BOX-V2", *Eur. Phys. J. C* **74** (2014), no. 1, 2702, doi:10.1140/epjc/s10052-013-2702-5, arXiv:1311.1365.

[40] T. Sjöstrand, S. Mrenna, and P. Skands, "PYTHIA 6.4 physics and manual", *JHEP* **05** (2006) 026, doi:10.1088/1126-6708/2006/05/026, arXiv:hep-ph/0603175.

[41] T. Sjostrand, S. Mrenna, and P. Z. Skands, "A Brief Introduction to PYTHIA 8.1", *Comput. Phys. Commun.* **178** (2008) 852–867, doi:10.1016/j.cpc.2008.01.036, arXiv:0710.3820.

[42] GEANT4 Collaboration, "GEANT4: A Simulation toolkit", *Nucl.Instrum.Meth. A* **506** (2003) 250, doi:10.1016/S0168-9002(03)01368-8.

[43] G. Bozzi et al., "Production of Drell-Yan lepton pairs in hadron collisions: Transverse-momentum resummation at next-to-next-to-leading logarithmic accuracy", *Phys. Lett. B* **696** (2011) 207, doi:10.1016/j.physletb.2010.12.024, arXiv:1007.2351.

[44] T. Gehrmann et al., "W^+W^- Production at Hadron Colliders in Next to Next to Leading Order QCD", *Phys. Rev. Lett.* **113** (2014), no. 21, 212001, doi:10.1103/PhysRevLett.113.212001, arXiv:1408.5243.

[45] C. Borschensky et al., "Squark and gluino production cross sections in pp collisions at $\sqrt{s}$ = 13, 14, 33 and 100 TeV", *Eur. Phys. J. C* **74** (2014), no. 12, 3174, doi:10.1140/epjc/s10052-014-3174-y, arXiv:1407.5066.

[46] B. Fuks, M. Klasen, D. R. Lamprea, and M. Rothering, "Gaugino production in proton-proton collisions at a center-of-mass energy of 8 TeV", *JHEP* **10** (2012) 081, doi:10.1007/JHEP10(2012)081, arXiv:1207.2159.

[47] B. Fuks, M. Klasen, D. R. Lamprea, and M. Rothering, "Precision predictions for electroweak superpartner production at hadron colliders with RESUMMINO", *Eur. Phys. J. C* **73** (2013) 2480, doi:10.1140/epjc/s10052-013-2480-0, arXiv:1304.0790.

[48] W. Beenakker et al., "The Production of charginos / neutralinos and sleptons at hadron colliders", *Phys. Rev. Lett.* **83** (1999) 3780–3783, doi:10.1103/PhysRevLett.100.029901,10.1103/PhysRevLett.83.3780, arXiv:hep-ph/9906298. [Erratum: Phys. Rev. Lett.100,029901(2008)].

[49] CMS Collaboration, "Measurement of the inclusive top-quark pair + photon production cross section in the muon + jets channel in pp collisions at 8 TeV", CMS Physics Analysis Summary CMS-PAS-TOP-13-011, CERN, Geneva, 2014.

[50] CMS Collaboration, "Measurement of the WW cross section pp collisions at sqrt(s)=13 TeV", CMS Physics Analysis Summary CMS-PAS-SMP-16-006, CERN, Geneva, 2016.

[51] CMS Collaboration, "Measurement of the WZ production cross section in pp collisions at sqrt(s) = 13 TeV", CMS Physics Analysis Summary CMS-PAS-SMP-16-002, CERN, Geneva, 2016.

[52] CMS Collaboration, "Measurement of the ZZ production cross section and $Z \to \ell\ell\ell'\ell'$ branching fraction in pp collisions at $\sqrt{s} = 13$ TeV", CMS Physics Analysis Summary CMS-PAS-SMP-16-001, CERN, Geneva, 2016.

[53] T. Junk, "Confidence level computation for combining searches with small statistics", *Nucl.Instrum.Meth. A* **434** (1999) 435, arXiv:hep-ex/9902006.

[54] A. L. Read, "Presentation of search results: the CLs technique", *J. Phys. G* **28** (2002) 2693, doi:10.1088/0954-3899/28/10/313.

[55] ATLAS Collaboration, CMS Collaboration, LHC Higgs Combination Group Collaboration, "Procedure for the LHC Higgs boson search combination in Summer 2011", CMS-NOTE-2011-005. ATL-PHYS-PUB-2011-11, CERN, Geneva, Aug, 2011.

[56] E. Gross and O. Vitells, "Trial factors or the look elsewhere effect in high energy physics", *Eur. Phys. J. C* **70** (2010) 525, doi:10.1140/epjc/s10052-010-1470-8, arXiv:1005.1891.

[57] CMS Collaboration, "Search for supersymmetry in events with photons and missing transverse energy", CMS Physics Analysis Summary CMS-PAS-SUS-15-012, CERN, Geneva, 2016.